The Journal of Chemical Physics ARTICLE pubs.aip.org/aip/jcp

Ultrafast internal conversion and photochromism in gas-phase salicylideneaniline

Cite as: J. Chem. Phys. 159, 104304 (2023); doi: 10.1063/5.0161238
Submitted: 8 June 2023 • Accepted: 11 August 2023 •
Published Online: 8 September 2023

Myles C. Silfies,[1] Arshad Mehmood,[2,3] Grzegorz Kowzan,[2,4] Edward G. Hohenstein,[5] Benjamin G. Levine,[2,3] and Thomas K. Allison[1,2,a)]

AFFILIATIONS

[1] Department of Physics and Astronomy, Stony Brook University, Stony Brook, New York 11794, USA
[2] Department of Chemistry, Stony Brook University, Stony Brook, New York 11794, USA
[3] Institute for Advanced Computational Science, Stony Brook University, Stony Brook, New York 11794, USA
[4] Institute of Physics, Faculty of Physics, Astronomy and Informatics, Nicolaus Copernicus University in Toruń, ul. Grudziadzka 5, 87-100 Toruń, Poland
[5] QC Ware Corporation, Palo Alto, California 94301, USA

[a)] **Author to whom correspondence should be addressed:** thomas.allison@stonybrook.edu

ABSTRACT

Salicylideneaniline (SA) is an archetypal system for excited-state intramolecular proton transfer (ESIPT) in non-planar systems. Multiple channels for relaxation involving both the keto and enol forms have been proposed after excitation to S_1 with near-UV light. Here, we present transient absorption measurements of hot gas-phase SA, jet-cooled SA, and SA in Ar clusters using cavity-enhanced transient absorption spectroscopy (CE-TAS). Assignment of the spectra is aided by simulated TAS spectra, computed by applying time-dependent complete active space configuration interaction (TD-CASCI) to structures drawn from nonadiabatic molecular dynamics simulations. We find prompt ESIPT in all conditions followed by the rapid generation of the trans keto metastable photochrome state and fluorescent keto state in parallel. Increasing the internal energy increases the photochrome yield and decreases the fluorescent yield and fluorescent state lifetime observed in TAS. In Ar clusters, internal conversion of SA is severely hindered, but the photochrome yield is unchanged. Taken together, these results are consistent with the photochrome being produced via the vibrationally excited keto population after ESIPT.

I. INTRODUCTION

Tracking and understanding the redistribution of internal energy has been one of the main goals of ultrafast spectroscopy since its inception. In photochromic molecules, the absorption of light causes large electronic reorganization, leading to a reversible change in absorption and a corresponding material color change.[1] Often, these changes are driven by excited state intramolecular proton transfer (ESIPT) reactions and/or rapid isomerization on sub-picosecond timescales, requiring ultrafast techniques to follow the dynamics. Additionally, in the case of ESIPT, the redistribution of energy results in a large (~1 eV) Stokes shifted fluorescence.[2,3] Recently, there has been a significant amount of work to use photochromic and/or ESIPT molecules in applications such as textiles,[4] optical memories,[5,6] and sensors.[7–9]

Even as the absorption and emission shifts found in ESIPT/photochromic materials are now being exploited for consumer and industrial applications, many foundational spectroscopy studies continue on increasingly larger systems as well as in the closely related field of proton-coupled electron transfer (PCET).[10,11] As the complexity of the molecule increases, so does the difficulty in understanding the relaxation dynamics and potential photochromism mediated by proton or hydrogen transfer as opposed to internal conversion mediated by other degrees of freedom. One of the most studied photochromic systems exhibiting competing dynamic pathways is the archetypal Schiff base salicylideneaniline (SA) depicted in Fig. 1. In solution and solid phases, SA becomes red after irradiation with UV light and remains trapped in this metastable state that can be reversed via irradiation by blue light.[12–15] Spectroscopically, this "photochrome state" is observable as a pho-

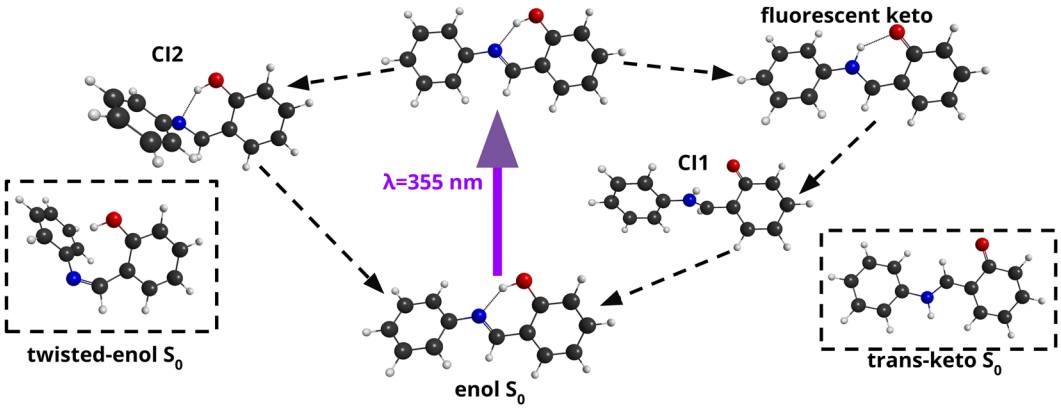

FIG. 1. General overview of relaxation schemes for SA excited to S_1. After excitation, the excited enol can either (right side) undergo ESIPT and internally convert along the keto pathway through CI1 or (left side) remain in the enol tautomer and relax via CI2 by rotating about the central C–N bond. Bottom left and right insets are alternative ground state minima that are potential photochrome geometries, which may be reached via the enol or keto relaxation pathways, respectively.

toinduced, long-lived absorption feature most likely due to a trapped population of an isomerized ground state geometry.

Although still under debate, the general photoinduced relaxation scheme has been recently summarized and improved by Pijeau *et al.* with high-level dynamics simulations,[16] which built off of earlier work.[17–19] This scheme, shown in Fig. 1, is described as follows. In the ground state, SA is in the enol form and nonplanar with a ≈35° – 50° twist around the anilino C–N bond depending on the level of theory or experimental data.[16–18,20] Theory indicates that the barrier to proton transfer is lower with decreasing twist angles, and ESIPT is more likely to occur from planar geometries.[16–18,21] Therefore, upon UV excitation to the $S_1(\pi,\pi*)$ state ($\lambda_{max} \approx 350$ nm), SA must first planarize before undergoing ESIPT to form the excited keto form. However, the ground state potential energy only weakly depends on the anilino C–N twist angle, so even at low temperatures, there is a nonzero probability of planar geometries.[21]

The keto form populated after ESIPT can relax via a number of channels, with sequencing and branching ratios not well understood or agreed upon. Spectroscopic signals indicate that a portion of molecules decay radiatively from a fluorescent keto form or become trapped in a long-lived photochromic state, which absorbs blue light as described above. Additionally, some population of excited molecules can undergo internal conversion back to the ground state via a conical intersection (CI) followed by ground-state back proton transfer. The keto CI, labeled "CI1" in Fig. 1, was found theoretically and requires a rotation of nearly 90° around the phenolic C–C bond.[16] Using DFT calculations, Ortiz-Sánchez *et al.* found the ground state keto minimum structure shown on the bottom right of Fig. 1, which has a full 180° rotation about the same phenolic bond, and this is widely accepted as the photochrome geometry.[17,22–24]

Additionally, due to the nonplanar structure, a competing relaxation channel involving the excited enol without ESIPT has been proposed.[16–18] This pathway, shown on the left side of Fig. 1, requires a large internal twist of 90° around the central C–N bond to reach CI2 and relax to the ground state. A secondary enol ground state minimum was found along this trajectory and is shown in the bottom left of Fig. 1. This twisted enol geometry is also a candidate for the photochromic state, especially if excited with higher energy light.[17,23,25] Pijeau *et al.* investigated the branching ratios and internal conversion rates of the two main channels and found that 80% of the excited-state population relaxes via CI1 after ESIPT within 800 fs and 20% via the enol CN twist channel in ≈250 fs.[16]

SA has been studied using a variety of ultrafast techniques to observe the competing reaction dynamics and determine the nature of the various decay channels. Mitra and Tamai recorded the first femtosecond transient absorption spectra (TAS) in various solvents and found an instrument-limited proton transfer time and a monoexponential decay of both excited-state absorption (ESA) and stimulated emission (SE) with 4 ps time constant in cyclohexane, as well as a long-lived signal assigned to the photochrome.[26,27] They proposed, like many of the early studies,[15,28] that the initially hot keto state relaxes into either a relaxed fluorescing keto or the photochrome within the first several hundred fs and then the fluorescent state undergoes internal conversion on the picosecond time scale, with the lifetime depending on solvent environment. TAS measurements by Ziółek *et al.* further refined the proton transfer time to <50 fs and an excited state relaxation time constant of 7 ps in acetonitrile.[29] Their interpretation finds a sequential model along the keto channel with the photochrome evolving from the relaxed keto state in competition with back-proton transfer on the ground state, disagreeing with previous work. Fluorescence upconversion measurements in acetonitrile also agree with this model.[30]

In the gas phase, Sekikawa *et al.* performed time-resolved photoelectron spectroscopy (TRPES) in a helium seeded molecular beam.[21] Their results agreed with the solution TAS work on the ESIPT timescale being $\lesssim$ 50 fs but found that the intermediate decay time constant was 1.2 ps, which was assigned to a combination of the ESIPT and CN twist channels. They also observed a long-lived feature, which they assigned as the trans keto photochrome but suggested that the isomerization occurs in the excited state. To further understand the dynamics, the authors performed tunable pump measurements, which will be discussed in Sec. IV in comparison to our results. In general, it is difficult to determine if the

lack of agreement between TAS and TRPES is due to the observable (optical absorption vs photoionization) or the environment (solution vs gas phase), and this is particularly true for a molecule with many competing relaxation channels, such as SA.

In this article, we address the dynamics of salicylideneaniline after excitation to S_1 with $\lambda = 355$ nm using a combination of cavity-enhanced transient absorption spectroscopy (CE-TAS) and quantum chemistry/molecular dynamics calculations that directly simulate the observable. CE-TAS[31,32] uses a combination of high-power fibers lasers[33] and tunable cavity-enhanced frequency combs[34,35] for broadband transient absorption measurements in dilute molecular beams. CE-TAS acts as a halfway point between TAS and TRPES—sharing the observable of the former and the environment(s) of the latter. By varying the molecular beam conditions, we record dynamics of vibrationally hot SA (420 K), jet-cooled SA, and SA embedded in Ar clusters. We directly compare the CE-TAS measurements to calculations of the transient absorption spectra using a newly developed real time time-dependent complete active space configuration interaction (TD-CASCI) technique.[36,37]

Overall, we find stronger agreement with the results of previous solution-phase TAS studies than the conclusions of gas-phase studies based on photoionization. We find prompt ESIPT after photoexcitation and relaxation dynamics in accordance with the previously proposed keto channels under all our studied conditions. We do not observe any evidence of the CN twist channel within our detection window, but cannot rule it out completely as we calculate that the TAS signal for this channel should lie to the blue of our shortest 450 nm wavelength. Most strikingly, we find that for SA in Ar clusters, internal conversion of the fluorescent state is shut off, while the photochrome yield remains unchanged. This supports a parallel mechanism for fluorescence and the photochrome state. Comparing all the measurements and theory, we present a comprehensive picture of the keto relaxation channels of salicylideneaniline in Sec. IV.

II. METHODS

A. Experimental

SA was purchased from TCI chemicals (97%) and used as received. For all experiments, the sample is placed in a stainless steel cell and heated to 125 °C to increase the vapor pressure. Either He or Ar is used as carrier gas for a planar supersonic expansion from a 5 mm × 0.2 mm slit nozzle, as described previously.[31] Unless otherwise specified, the He stagnation pressure is 0.1 bar and the Ar stagnation pressure is 1 bar. For all measurements shown, the interaction region is 3 mm above the nozzle, well within the expansion's "zone of silence."[38]

The cavity-enhanced transient absorption spectrometer operating at a 100 MHz repetition rate used for all experiments is described in detail in Ref. 31 and in the supplementary material. The pump wavelength is 355 nm, and the cavity-enhanced probe wavelength is tunable from 450 to 700 nm.[34,35] The CE-TAS signal ΔS is constructed from subtraction of two signals from counter-propagating cavity-enhanced frequency combs delayed by $T_{pr} \approx 5$ ns, as described previously.[31,32] For pump/probe signals with much shorter lifetime than $1/f_{rep} = 10$ ns, the CE-TAS signal ΔS is the same as one would normally record in conventional transient absorption spectroscopy setups. However, for longer-lived signals, there are additional subtleties, which must be accounted for, and we discuss these in Sec. II B and in the supplementary material.

Unless otherwise stated, all data shown are magic angle signals constructed from signals recorded with pump and probe polarizations parallel ($\Delta S_\parallel$) and perpendicular ($\Delta S_\perp$) via $\Delta S_{MA} = (\Delta S_\parallel + 2\Delta S_\perp)/3$. All broadband spectra (e.g., Fig. 2) shown are built up piecewise from pump/probe scans at 10–12 discrete probe wavelengths, taking into account the wavelength-dependent cavity finesse. To generate contour plots from the individual scans, a marching squares algorithm is used for interpolation. In the case of data taken with large amounts of Ar carrier gas, producing Ar clusters around the SA molecules that suppresses internal conversion, signal amplitudes are scaled by fluorescence signals recorded independently during the pump/probe measurements.[31] For data taken with He carrier gas, the fluorescence signal was too weak for the current instrument sensitivity, so the data are unnormalized. However, when using He, the molecule pickup is more stable than in the Ar case, most likely due to the lower stagnation pressures and the lack of clustering, and we find good reproducibility across multiple datasets even without fluorescence normalization.

Since the previously measured ESIPT occurs below our instrument response of ≈200 fs,[21,29] fitting the rising edge of the signal to an error function is used for aligning time zero for each scan in the spectrum. We verified that the rising edge of the signal is, indeed, instrument-response-limited by separately measuring the instrument response function at several probe wavelengths using 2-photon absorption in gas-phase carbon disulfide immediately following an SA measurement (supplementary material, Fig. S11).

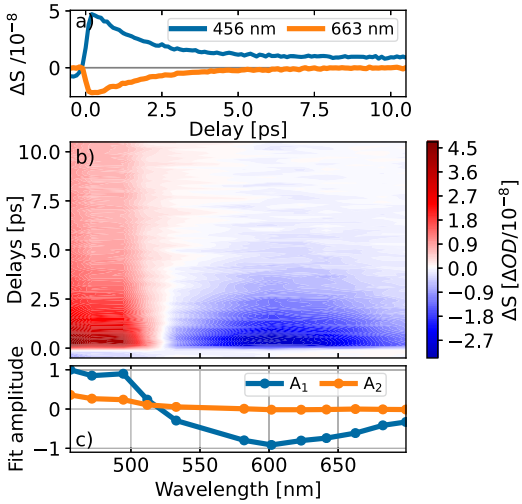

FIG. 2. CE-TAS of an isolated jet-cooled SA molecule. (a) Raw signals at two representative probe wavelengths. (b) TA spectrum constructed from the individual scans. (c) DAS from the global fit of (b) with two components, normalized to the maximum of A_1. A_1 and A_2 are associated with time constants of 1.8 ps and >10 ns, respectively. Individual points are at the discrete probe wavelengths, which are combined for the full spectrum. The origin and meaning of pre-time-zero signals are discussed in the text.

B. Modeling

A standard tool for analyzing transient absorption spectra is global analysis (GA),[39] in which the transient absorption signal is modeled as a sum of decay associated spectral (DAS) components $X_n(\lambda)$ each with its own exponential decay with characteristic time constant, τ_n, viz.,

$$G(\lambda, t) = \mathrm{IRF}(t) \otimes \sum_n X_n(\lambda) \exp(-t/\tau_n). \quad (1)$$

In Eq. (1), the GA model is convolved with a Gaussian instrument response function IRF(t). For many CE-TAS experiments on molecules with short-lived signals with $\tau \ll 1/f_{\mathrm{rep}}$, this standard GA model is sufficient since the CE-TAS signal ΔS is essentially the same as TA signals recorded by conventional transient absorption spectrometers. However, for data with long-lived components, with $\tau_n \gtrsim 1/f_{\mathrm{rep}}$, it is more appropriate to use a modified model that accounts for multiple excitation of the sample and reference-pulse subtraction in the following manner:

$$\Delta S_{\mathrm{model}}(\lambda, t) = \sum_{m=0}^{N} G(\lambda, t + m/f_{\mathrm{rep}}) - G(\lambda, t + m/f_{\mathrm{rep}} + T_{\mathrm{pr}}). \quad (2)$$

In Eqs. (1) and (2), $G(\lambda, t)$ represents the intrinsic molecular dynamics and $\Delta S_{\mathrm{model}}(\lambda, t)$ is the modeled CE-TAS signal. The time offset in the subtracted signal is due to the reference pulse reaching the sample T_{pr} before the probe. N is the approximate number of pump pulses that molecules see as they fly through the focus. For the modeling shown here, we use $N = 20$, but the DAS component is not sensitive to this choice as long as it is much larger than 1. Note that although the *sample* is excited by $\sim N$ pulses, as discussed in Ref. 31, the excitation density is sufficiently low that multiple excitation of the same *molecule* is negligible. All experimental data are modeled using Eq. (2), although for the isolated molecule with only one long-lived component, similar results are obtained using either (1) or (2). In addition, note that for modeling CE-TAS data, we use a wavelength dependent IRF. The fit parameters are optimized by minimizing the reduced χ^2 using a Levenberg–Marquardt global fitting algorithm. A parallel model is used because the proposed relaxation channels occur in parallel following the initial excitation and not in sequence. Additionally, any photochrome signature in the fit is sufficiently slow such that the DAS component for the photochrome does not depend on whether a parallel or sequential model is used.

C. Theoretical calculations

All the theoretical calculations presented in this study utilize the excited state trajectories derived from the previously published[16] molecular dynamics simulations conducted by one of the authors (EGH). Those calculations used the *ab initio* multiple spawning (AIMS) method[40,41] for modeling nonadiabatic molecular dynamics. The potential energy surfaces (PESs) were computed on-the-fly via a complete active space configuration interaction (CASCI) method, which employs a set of pre-determined orbitals to minimize computational costs and ensure the generation of well-behaved PES.[42] The orbitals were determined utilizing the Floating Occupation Molecular Orbital (FOMO) method[43–46] based on the Gaussian broadening of each orbital's energy level at an electronic temperature parameter β = 0.35 a.u. The FOMO temperature serves as a crucial empirical parameter, capable of precise calibration to attain the desired orbital characteristics and accuracy. When the temperature is excessively low, the FOMO orbitals regress to Hartree–Fock canonical orbitals, which inadequately describe electronic excited states. The dynamic electron correlation effects, which are neglected by the CASCI method, were incorporated by using the density functional theory embedding correction[47] with a ωPBEh functional.[48] An active space of two electrons in two orbitals was employed, which is adequately flexible to accurately describe the specific regions of interest on the S_1 potential energy surface. We will abbreviate this method ωPBEh-FOMO(0.35)-CAS(2,2)CI/6-31g**, going forward.

The direct calculation of the spectroscopic observables from *ab initio* molecular dynamics simulations enables more definitive assignments of spectral features than is possible by the indirect comparison of experimentally observed lifetimes to simulations.[49–53] The TAS signal is computed theoretically from AIMS simulations. A detailed description of the method for calculation of the TAS spectrum is included in the supplementary material, Sec. S3 B, so here, we provide only a short overview. Representative geometries are systematically drawn from AIMS simulations via a clustering algorithm. Specifically, 80 distinct conformations are sampled from each ≈24 fs window of the dynamics simulations for a total of 6720 structures. The ESA and SE are computed via three time-dependent (TD) CASCI method[37,54] simulations at each geometry, with light polarized in the x, y, and z directions, respectively. In doing, we take advantage of the fact that time-dependent electronic structure methods are a robust and efficient method to compute molecular absorption spectra.[55–59] Previous studies[37] conducted by one of the authors (BGL) have established that TD-CASCI presents numerous advantages in comparison to the commonly employed real-time time-dependent density functional theory, and its implementations for the modern computational hardware allow us to use thousands of geometries to simulate TAS at an affordable cost. To adequately account for the excitations to the higher excited states, a larger (8,8) active space is used to calculate the TAS spectrum, and to avoid possible convergence failure with employed active space, the FOMO temperature was reduced to 0.25 a.u., with the other parameters of the electronic structure method as described above for the dynamics (ωPBEh-FOMO(0.25)-TD-CAS(8,8)CI/6-31g**). The electronic wavefunctions at each geometry are excited by a δ function pulse and then propagated for 45 fs with a 0.003 fs steps. Fourier transforms of the resulting correlation functions provide spectra with a spectral resolution of 0.11 eV ($\Delta\lambda$ = 28 nm at λ = 450 nm; $\Delta\lambda$ = 74 nm at λ = 700 nm). The ESA and SE signals are separately shifted by +0.944 and −1.595 eV, respectively, to better agree with more trustworthy complete active space second-order perturbation theory calculations of ESA and the experimental absorption maximum,[27] respectively. In total, the spectra presented required the simulation of 0.9 ns of electron dynamics, which was enabled by our previously reported GPU-accelerated direct TD-CASCI algorithm.[37] All electronic structure calculations were carried out using the TeraChem software package.[60–62] Additional methodological details can be found in the supplementary material, and a separate paper focused on the theoretical method for computing TAS is forthcoming.[36]

To facilitate a comparison with the experiment, we process the theoretical TAS results in a manner analogous to how the experiment is performed and analyzed. First, the theoretical TAS data from the AIMS/TD-CASCI are sampled at points with 15 nm spacing with a 3 THz FWHM instrument response, which approximately corresponds to the intracavity bandwidth with which each experimental TA trace is recorded. The sampled dataset is then further convolved with a 200 fs FWHM Gaussian in time.

Several sources of error are present in these calculations: statistical error arising from trajectory sampling, as well as error inherent to the electronic structure and dynamics simulation methods. We estimate that the majority of the error is associated with physical approximation, not sampling. However, quantifying statistical error is not practical because the application of a clustering algorithm prior to computing the probe prevents us from separating the computed signal into contributions from individual trajectories without performing a large number of additional electronic structure calculations.

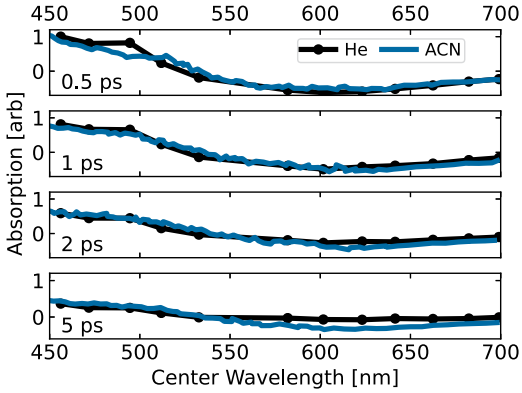

FIG. 3. Lineout comparison between TAS of the jet-cooled SA molecule and in SA in acetonitrile (ACN) for different delay times. One global scaling factor is used between the two datasets at all times. ACN data from Ref. 29.

III. RESULTS

A. The isolated molecule

The TA of SA cooled in He carrier gas is shown in Fig. 2. Representative pump/probe scans are shown in Fig. 2(a), and the full TA spectrum is shown in Fig. 2(b). Note that the negative ΔS at negative time delays is due to long-lived excited-state absorption in the signal on the blue side of the spectrum. The origin of this pre time-zero signal is illustrated with examples in the supplementary material. This negative delay ΔS signal provides information on long-lived components of the true TA signals, and these long-lived DAS components are extracted via modeling the full signal (i.e., both negative and positive delays) as discussed in Sec. II B.

The SA ground-state minimum does not absorb in the visible range; therefore, no bleach signal is considered,[27] i.e., all negative signals are from stimulated emission. From modeling of the decay of the polarization anisotropy (i.e., the weighted difference between signals recorded with parallel and perpendicular relative polarizations) using the procedure of Felker *et al.*,[63] we estimate the rotational temperature in the expansion to be 80 K, well above the condensation temperature of He, such that no clustering in the helium expansion is expected or observed.

We fit the data using Eqs. (1) and (2) with $X_n \equiv A_n$. The DAS components for the isolated SA are shown in Fig. 2(c) for GA with two time constants (reduced $\chi^2 = 1.9$). The associated time constants are $\tau_{A_1} = 1.8$ ps and $\tau_{A_2} > 10$ ns. The points shown on the DAS component are the discrete probe wavelengths that make up the spectrum. The same fit procedure was also tested for one (reduced $\chi^2 = 51.5$) and three (reduced $\chi^2 = 2.7$) components.

The short-lived A_1 is composed of both negative and positive features in the spectrum, indicating excited state absorption (ESA) and stimulated emission (SE) from the same state, and is the typical type of TAS signature seen for excited-state proton transfer in many molecules.[64–67] The 1.8 ps time constant lies between those reported for gas-phase TRPES[21] and solution-phase TAS.[26,27,29] The long-lived A_2 extends out from the blue edge of the spectrum, is only positive, and remains nearly constant out to the maximum delay of the instrument (700 ps). In the raw pump–probe traces, A_2 also appears as a negative signal for wavelengths less than 530 nm, which is accounted for in the model, as described in Sec. II B. This feature is most likely ground-state absorption from the long-lived photochromic state observed in numerous previous experiments. The assignment and origin of this state are further discussed in Sec. IV.

In Fig. 3, we compare our TA spectra to those reported by Ziółek *et al.*[29] for SA excited at $\lambda = 390$ nm in acetonitrile. The data shown have only a single global scaling to overlap the bluest probe value at 0.5 ps, and this scale factor is applied to all the gas-phase data. The spectra show remarkable similarity, without even a solvatochromic shift. Additionally, Mitra and Tamai also measured solution-phase fs TAS of SA in several solvents and there are only minor spectral shifts between their data and our gas-phase measurements.[26,27]

While we do not vary the excitation energy in our experiments, we do vary the initial vibrational energy via coarse control of the temperature. The nozzle is held at 155 °C, and for an effusive beam (i.e., no carrier gas) or very low carrier gas stagnation pressures (quasi-effusive beam) such that there is no supersonic expansion, we expect the molecular temperature in the beam to be approximately the same as the nozzle. In practice, we find the SA density in the beam to be more stable for quasi-effusive beam and record "hot SA" data with 0.02 bar stagnation pressure of He. We have verified that identical dynamics are obtained with a quasi-effusive beam and with no carrier gas, and analyzing the rotational anisotropy, we find a rotational temperature for "hot SA" of 420 ± 20 K for the quasi-effusive beam, consistent with the nozzle temperature.

Figure 4 compares pump/probe traces for "hot SA" with the quasi-effusive beam and "cold SA" recorded with a He stagnation pressure of 0.1 bar. Higher He stagnation pressures do not alter the signal significantly. The vibrationally hot molecule decays slightly faster and shows a slightly larger amplitude for the long-lived signal.

B. Salicylideneaniline in argon clusters

To further understand the different parallel relaxation channels of SA, we perform experiments on SA in Ar clusters, which we denote as SA:Ar. Similar to a rare-gas matrix environment, Ar clustering can affect the dynamics in two ways: (1) by providing a

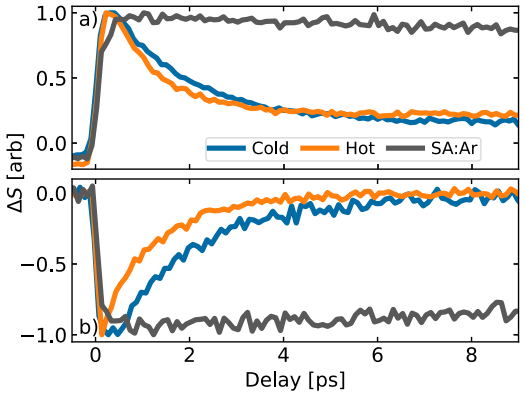

FIG. 4. Comparison of SA dynamics under different molecular beam conditions. "Cold" data are taken with 0.1 bar He stagnation pressure, giving a supersonic expansion and jet-cooled molecules. "Hot" data are recorded from a quasi-effusive beam. The SA:Ar data are taken with 1 bar Ar stagnation pressure, forming large Ar clusters. (a) λ_{probe} = 490 nm. (b) λ_{probe} = 616 nm.

channel for the dissipation of vibrational energy and (2) by providing steric hindrance to large amplitude motions, such as the isomerizations shown in Fig. 1. Figure 4 compares the CE-TAS signals for the SA:Ar system to the isolated molecule. The SA:Ar signal decays much slower in the clustered sample than in the hot or cold SA case. From our fluorescence measurements, we can place a lower bound on the enhancement of the total fluorescence yield of SA:Ar vs isolated SA of 100x. Fluorescence enhancement in SA has also been previously reported in matrix isolation studies.[28] The data in Fig. 4 were recorded at 1 bar since this provided a workable, stable signal for recording a full spectrum. Increasing the Ar pressure continues to enhance this effect until the pump/probe signal is nearly constant out to 700 ps at a stagnation pressure of 2.5 bar.

We estimate the average cluster size by analyzing the rotational anisotropy. Figure 5 compares $\Delta S_{\parallel}$, $\Delta S_{\perp}$ data taken in a He expansion to an Ar expansion with 1 bar stagnation pressure. The rotational anisotropy persists roughly 5 times longer due to the increased moment of inertia of the SA:Ar system. Considering that the rotational dephasing time scales as $1/\sqrt{B}$,[63] where B is the

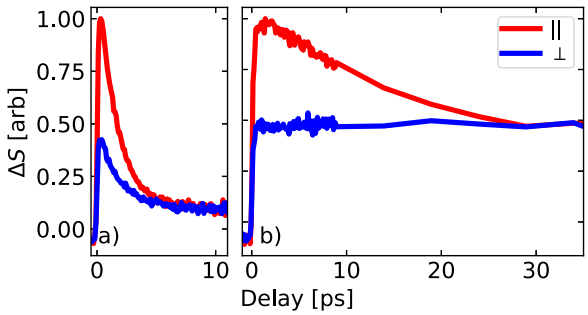

FIG. 5. Rotational dynamics of isolated SA vs SA:Ar. CE-TAS signals with pump and probe pulses parallel (red) and perpendicular (blue) for (a) isolated jet-cooled SA and (b) SA:Ar with 1 bar Ar stagnation pressure. λ_{probe} = 490 nm. Formation of large Ar clusters around the SA molecules dramatically slows rotational dephasing.

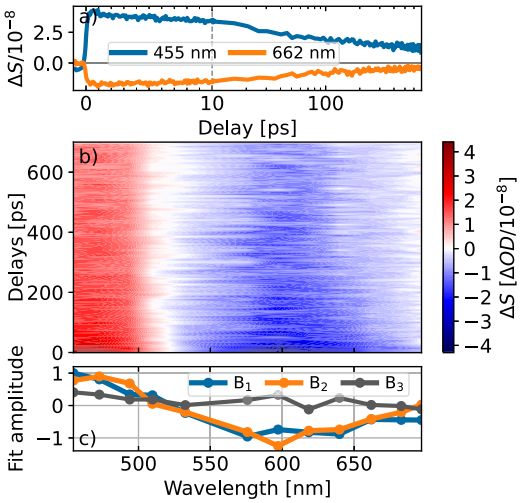

FIG. 6. CE-TAS of SA:Ar from SA seeded in 1 bar of Ar. (a) Pump/probe traces at two representative probe wavelengths. The time axis shown changes from linear to logarithmic at 10 ps to better show the signal at the negative time delays. (b) TA spectrum constructed from the individual scans. (c) DAS from the global fit of (b) with three components normalized to the maximum of B_1. τ_{B_1} = 24 ps, τ_{B_2} = 850 ps, and τ_{B_3} > 10 ns. Individual points are at the discrete probe wavelengths which were combined for the spectrum.

rotational constant, we estimate an average number of 15 Ar atoms clustered to the SA molecules.[68]

A full CE-TAS dataset for the SA:Ar system is shown in Fig. 6 with representative scans shown in Fig. 6(a) and the full spectrum in Fig. 6(b). Just as in the case of the individual lineouts discussed above, the entire spectrum decays with a significantly longer time constant than in the cold SA case above. Despite the slower decay, the initial rise time remains instrument response limited, indicating rapid ESIPT rates unaffected by the cluster environment.

We fit the data using Eqs. (1) and (2) with $X_n \equiv B_n$. The DAS components from the fit are shown in Fig. 6(c) for three components (reduced χ^2 = 4.2). The associated time constants are τ_{B_1} = 32 ps, τ_{B_2} = 1030 ps, and τ_{B_3} >10 ns. The same fit procedure was also tested for two (reduced χ^2 = 5.0) and four (reduced χ^2 = 4.1) time constants. The four-component fit is shown in the supplementary material (Fig. S8). The additional DAS component for the four-component fit has only a small amplitude at all wavelengths and a long decay time not apparent in the raw data, and thus, it was determined to be not significant. In general, the fits on the SA:Ar data are worse than the He case due to increased noise from turbulence from the higher pressure gas and scatter from bare Ar clusters.

The overall shapes of the DAS component are nearly identical to the He case in Fig. 2(b), indicating that the clustering is not modifying the electronic energies significantly. The only major change in the fit results is the additional component B_1. B_1 and B_2 are nearly identical to each other and to A_1, which most likely indicates that the monoexponential A_1 feature in cold SA becomes a biexponential $B_1 \rightarrow B_2$ decay in SA:Ar. Previous fluorescence measurements in matrix isolation also observed a biexponential decay in the fluorescence.[28]

C. Simulated spectrum

The simulated TAS spectrum is represented in Fig. 7(a). The raw theoretical data are presented in the supplementary material, Fig. S12. Just as for the experimental data, a global fit was applied to the theoretical data, with $X_n \equiv C_n$ in Eq. (1). Figure 7(d) shows the DAS component from a global fit to the data with two components. The associated time constants are $\tau_{C_1} = 0.62$ ps and $\tau_{C_2} = 20$ fs. Removing or adding components resulted in either a poor or non-physical (i.e., two nearly identical time constants) fit. The trajectories in AIMS simulations performed by Pijeau *et al.* were ended once the initial S_1 wavepacket population decayed below 0.01, so there is no contribution of trajectories on the ground-state surface to the spectrum.[16] Importantly, this means that the photochrome signal is not present in the simulated TAS dataset, but we address this drawback with static calculations discussed below.

A major benefit of directly computing experimental observables from theoretical trajectory data is that it is possible to analyze the spectrum by decomposing it into contributions that correspond to different molecular structures. To analyze the signature of proton transfer, we separate the spectrum into contributions from only keto or enol geometries by comparing O–H and N–H distances along the proton transfer coordinate. When $d_{O\text{-}H} - d_{N\text{-}H}$ is positive (negative), these geometries are labeled enol (keto). The spectral contributions from the keto and enol tautomers are shown in Figs. 7(b) and 7(c), respectively. For comparison with the DAS component of Fig. 7(d), we plot lineouts of the spectra at 100 fs in Figs. 7(e) and 7(f). From this comparison, it is clear that the C_1 DAS component corresponds to the keto spectrum after ESIPT.

C_2 in Figs. 7(d) and 7(f) is entirely negative across most of the spectrum representing prompt, broadband stimulated emission from enol tautomers during only the first ≈100 fs. The C_2 component corresponds well with the prompt enol geometry signal seen in Fig. 7(f), corresponding to near-planar enol geometries before and during ESIPT.

To further understand the spectral contribution from the CN twist relaxation mechanism, we filter the enol-only spectrum by CN twist angle, shown in the supplementary material, Fig. S13, for signals from geometries with angles less than 140°. In the ground state, this angle is 180° for a planar orientation and ≈90° near CI2,[16,17] so any features in the supplementary material, Fig. S13, should be signatures of the internal conversion toward CI2. Within the experimental observation window of 450–700 nm, all absorption or emission features from twisted enol geometries are more than an order of magnitude smaller than the main spectral components in Fig. 7(a). Thus, the CN twist channel may be present, but it is unlikely discernible in the TAS signal.

Separate from the AIMS/TD-CASCI calculations, we perform several TD-CASCI calculations at fixed geometries for the ground state local minima found by Ortiz-Sánchez *et al.*[17] The calculated absorption spectra for both prospective photochrome conformers are included in the supplementary material, Fig. S14. Our calculated trans keto photochrome (shown in the bottom right box of Fig. 1) spectrum has an absorption peak centered near 480 nm. We also calculate the absorption spectrum of Ortiz-Sánchez's twisted enol minimum (shown in the bottom left box of Fig. 1) and found absorbance at ≈300 nm, which is beyond the range probed in this experiment.

IV. DISCUSSION

Our overall proposed scheme for dynamics in both the isolated molecule and SA:Ar is shown in Fig. 8. Much of the dynamics is born out in the global analysis of the TA spectrum, which we describe step by step below.

In the isolated molecule, the initially excited enol quickly undergoes ESIPT, giving rise to the classic ESA/SE signature seen in the GA component A_1. We assign A_1 to the fluorescent keto state, and this assignment is consistent with the theory component C_1 and the keto-filtered theory data of Fig. 7(b). This assignment is also in accord with previous work on SA and other ESIPT molecules. At longer delays, after the fluorescent state has decayed, we assign the remaining long-lived signal, captured by A_2, to the

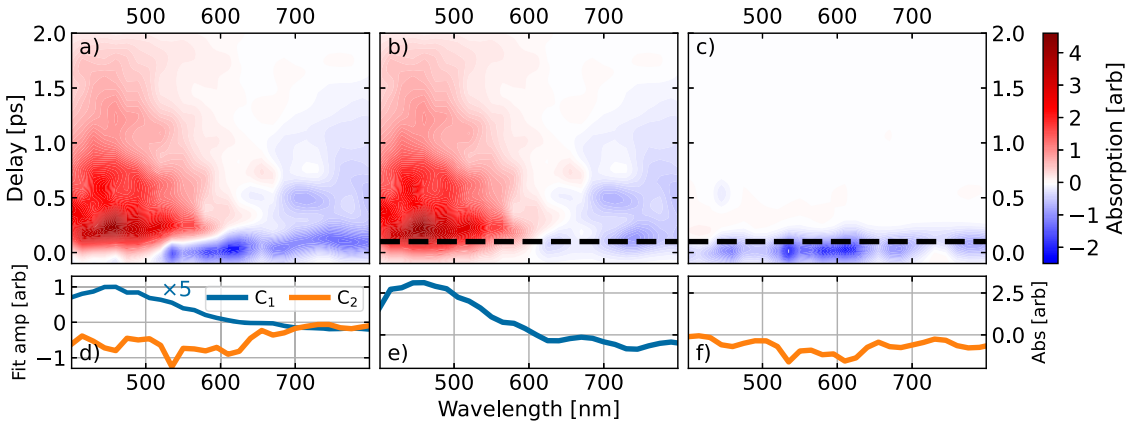

FIG. 7. Theoretical TAS results from post-processed AIMS calculations containing (a) all geometries, (b) only keto geometries, and (c) only enol geometries. (d) DAS from a global fit of the spectrum in (a). (e) and (f) Spectral lineouts using the right axis at 100 fs from the corresponding keto and enol spectra, respectively. See the text for details regarding resampling and convolution with experimental resolution.

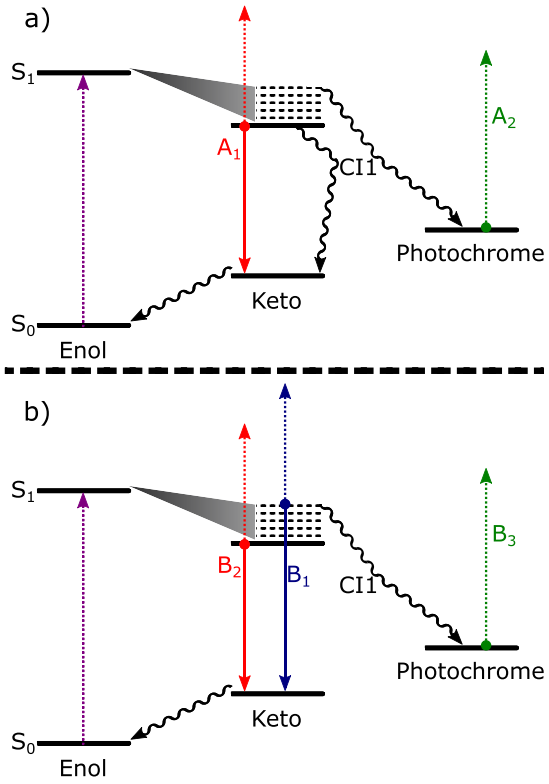

FIG. 8. Proposed relaxation mechanism and photochrome pathway in (a) isolated SA and (b) SA:Ar. Dashed lines indicate absorption of light and solid lines are emission. Labels indicate DAS features from global analysis. In the isolated molecule (a), the initially excited enol undergoes ESIPT and generates the keto tautomer with a wide range of internal energies. The hottest of which immediately internally convert to CI1 and isomerize to the photochrome. The colder population in the relaxed fluorescent state also decays via CI1, but eventually returns to the overall enol ground state. In SA:Ar (b), the presence of the Ar cage slows down photochrome generation (~0 → 24 ps) and traps the vibrationally cold keto population such that it can only decay radiatively (1.8 ps →> 1 ns).

keto photochrome. This assignment is supported by the correspondence between A_2 and other reported spectra of the metastable photochrome state[13–15,25,27,29] and also our calculated absorption spectrum for the trans keto minimum. We do not observe any signatures of the initially excited enol [C_2 and Fig. 7(c)] in the experimental data, most likely due to our time resolution and excess pump energy, but we do note that it was observed in solution by fluorescence upconversion.[30]

The 1.8 ps decay time of the excited keto state we observe is significantly slower than those observed in gas-phase TRPES by Sekikawa *et al.*[21] This highlights the role of the observable on the measured dynamics since nominally these two measurements are taken under the same molecule and excitation conditions. The shorter lifetime measured by TRPES could be due to energy windowing effects,[49,69,70] especially since the TRPES study was done using 1 + 2 photoionization.[21]

Comparing to solution phase work, the gas-phase TA spectra very closely correspond to those measured in solution, as shown in the raw data in Fig. 3. This is not unexpected since the TA spectrum shape has been previously shown to be relatively insensitive to the choice of solvent.[26,27] Regarding the dynamics, our 1.8 ps time constant is slightly shorter than the shortest S_1 keto lifetimes reported in solution phase work. A range of solution-phase lifetimes measured via TAS between 3.5 and 50 ps have been previously reported, with a strong solvent dependence.[26,27,29] The faster internal conversion in the absence of solvent supports the mechanism of internal conversion occurring at geometries very twisted compared to the ground state, as solvent can impede or slow down this large-amplitude motion.

Previous gas-phase experiments on SA varied the internal energy by changing the excitation wavelength. Sekikawa *et al.* observed a larger long-lived photochrome signal as the excitation energy was increased and assigned this feature to enhanced ESIPT with larger excitation energy due to barriers to ESIPT at twisted geometries.[21] In our experiment, we vary the internal energy of the molecule via large changes in temperature. Notably, we find that the appearance of the fluorescent keto signal (A_1) is equally prompt for both the hot SA and cold SA, as shown in Fig. 4, and thus, we find no evidence for a delay in the ESIPT at lower internal energies. However, we do find that the photochrome yield is higher for the vibrationally excited molecule, in accord with Sekikawa *et al.* We attribute this latter effect to the photochrome being formed from vibrationally excited keto molecules, as illustrated in Fig. 8(a). This was previously proposed by Rosenfeld *et al.*[14] and others,[15,18,27,28] but has since been disputed.[21,25,29] This conclusion is further supported by the impact of Ar clustering on the dynamics as discussed below.

While the clustering of SA with Ar has dramatic changes on the observed *dynamics* of the fluorescent state, captured by GA components B_1 and B_2, the *spectrum* of the fluorescent keto state is essentially unchanged. This is not unexpected, given the weak solvent dependence observed in previous TA work.[26,27] Our justifications for assigning B_1 and B_2 to the excited keto are the same as discussed in the isolated molecule, namely, correspondence with theory and previous work. The keto lifetime increases from 1.8 ps to a biexponential decay with τ_{B_1} = 32 ps and τ_{B_2} = 1030 ps when measured with 1 bar Ar stagnation pressure. These lifetimes continue to increase with increasing Ar carrier pressure, which we attribute to increasing the fraction of SA molecules in the beam clustered with Ar.

As mentioned before, Ar clustering can affect the dynamics in two ways: (1) dissipation of vibrational energy and (2) steric hindrance of large amplitude motions. From the hot/cold comparison in the isolated molecule, where we observe only a small effect of vibrational energy of the dynamics, we conclude that the dominant effect is steric hindrance. Ar atoms clustered around the central bonds can inhibit the large rotation necessary to reach CI1. Similar overall trends were observed in SA in different environments using ps time-resolved fluorescence, with only minor changes (factors of 2–5) in lifetimes across a wide range of solvents and a few hundredfold increase in matrices and glasses.[28]

While the excited keto population giving rise to fluorescence is stabilized upon clustering with Ar, the photochrome yield we observe (captured by B_3), as judged by the ratio of the photochrome signal compared to the initial TAS signal amplitudes, is the same in SA:Ar as the isolated molecule. This strongly supports a parallel channel for the production of the photochrome, separate from

the relaxed fluorescent keto state. After ESIPT, keto geometries are formed with a wide range of internal energies. The B_1 and B_2 DAS components are very similar, indicating a similar electronic state and geometry, and we assign B_1 to the hotter portion of the keto population. The absence of a spectral shift between B_1 and B_2, i.e., B_2 is not a shifted IVR product of B_1, further supports a parallel model. In the proposed dynamic scheme of Fig. 8(b), the vibrationally more energetic population of keto geometries is formed promptly and reaches CI1 more easily. This "hotter" population can then continue to isomerize on the ground state to the trans keto photochrome state. Note that the initial internal energy is similar in the cold isolated and SA:Ar cases, and thus, the hot keto population fraction and photochrome yields are the same, whereas the photochrome yield for the hot isolated molecule is larger than both jet-cooled SA and SA:Ar.

The vibrationally cooler population, to which we assign to B_2, like A_1, represents the state responsible for fluorescence. Instead of forming the photochrome, this population returns to the ground state cis keto and, eventually, undergoes back proton transfer to the S_0 enol minimum. In this model, the initially excited enol is the common precursor to both channels that produce the photochrome and fluorescent state, as proposed by Zgierski and Grabowska.[18] Note that biexponential nature and hot keto population are not observed in the isolated molecule case because the hot population can go through CI1 and form the photochrome much more quickly, and this is not resolvable with our time resolution. The major difference between the isolated and SA:Ar cases, highlighted in Fig. 8, is the relaxation mechanism from the relaxed fluorescent state. In the isolated molecule, this decay to the ground state keto takes 1.8 ps and occurs predominantly via internal conversion to CI1 due to the short excited state lifetime and reduced fluorescence yield. In SA:Ar, the clustering shuts off the internal conversion pathway and forces radiative decay to be the dominant pathway, which we observe as an increase in fluorescence and excited state lifetime.

V. CONCLUSIONS

In this work, we have combined cavity-enhanced transient absorption spectroscopy with AIMS/TD-CASCI calculations to study the dynamics of salicylideneaniline after excitation to S_1. This study introduces several new paradigms in ultrafast spectroscopy. For one example, our experiments on SA in Ar clusters are analogous to matrix isolation, where ultrafast spectroscopy has previously been very difficult and limited mostly to "action"-based methods based on fluorescence detection.[71–73] Using the CE-TAS method, we have shown how one can effectively record conventional ultrafast transient absorption (i.e., direct absorption) measurements in rare-gas matrix environments with rapid sample refreshment. For another example, we have shown how long-lived TA signals with lifetime $\tau \gtrsim 1/f_{rep}$ can be recovered via careful analysis of data at negative pump/probe delays and the modified GA model of Eq. (2). These new techniques can be applicable for both future CE-TAS studies and other ultrafast spectroscopy contexts.

The TD-CASCI technique presented here allows for quickly simulating TAS spectra from AIMS calculations, which, when compared to experimental spectra, facilitate spectral assignment. Additionally, processing the simulated and experimentally measured data in an identical way further helped assign dynamics. With gas phase TAS measurements, we are measuring the free molecular dynamics, which makes direct simulation easier without the need for solvent models.

By combining these new experimental and theoretical techniques, we provide insights into the relaxation dynamics of SA, summarized in Fig. 8. In general, we find stronger agreement with the time constants and interpretations from previous solution-phase TAS work although we do agree with the trends found in TRPES. By comparing and contrasting with previous work and reinterpreting within the scope of our analysis, we hope to provide a more universal model. After prompt ESIPT, keto geometries are formed with a broad energy distribution, the hottest of which rapidly internally convert through CI1 and isomerize to the trans keto photochromic state. The colder keto population relaxes more slowly through CI1 to reach the cis keto ground state in 1.8 ps for the isolated molecule and eventually return to the enol S_0 minimum. Increasing the internal energy by lowering the gas pressure results in more hot keto population and more yield of the long-lived photochrome. Embedding the SA molecule in Ar clusters sterically hinders isomerization such that only the hot keto population can undergo internal conversion to the photochrome state, with a dramatic increase in the S_1 lifetime recorded in TAS and also the fluorescence yield. We find no experimental evidence for the proposed secondary enol twist relaxation channel, but our calculations indicate that it likely lies outside our detection window.

SUPPLEMENTARY MATERIAL

The supplementary material contains a detailed description of the signal processing and global analysis methodology, including fits with different numbers of components; a comparison of the independent instrument response function to the SA signal; and a description of the theoretical methodology, including twisted enol and photochrome absorption spectra.

ACKNOWLEDGMENTS

This work was supported by the American Chemical Society Petroleum Research Fund under Grant No. 62125-ND6, the U.S. National Science Foundation under Award No. 2102319, and the U.S. Air Force Office of Scientific Research under Grant No. FA9550-20-1-0259. GK acknowledges the support from the European Union's Horizon 2020 Research and Innovation Program under Marie Sklodowska-Curie Grant Agreement No 101028278. AM and BGL acknowledge the Institute for Advanced Computational Science and Stony Brook University for funding.

AUTHOR DECLARATIONS

Conflict of Interest

The authors have no conflicts to disclose.

Author Contributions

Myles C. Silfies: Conceptualization (equal); Formal analysis (equal); Investigation (equal); Methodology (equal); Writing – original draft

(equal); Writing – review & editing (equal). **Arshad Mehmood**: Formal analysis (equal); Methodology (equal); Software (equal); Writing – original draft (equal). **Grzegorz Kowzan**: Formal analysis (equal); Investigation (equal); Writing – review & editing (equal). **Edward G. Hohenstein**: Resources (equal). **Benjamin G. Levine**: Conceptualization (equal); Funding acquisition (equal); Methodology (equal); Project administration (equal); Supervision (equal); Writing – original draft (equal); Writing – review & editing (equal). **Thomas K. Allison**: Conceptualization (equal); Funding acquisition (equal); Methodology (equal); Project administration (equal); Supervision (equal); Writing – original draft (equal); Writing – review & editing (equal).

DATA AVAILABILITY

The data that support the findings of this study are available from the corresponding author upon reasonable request.

REFERENCES

[1] K. Uchida, "Photochromism. Molecules and systems. Edited by Heinz Dürr and Henri Bouas-Laurent," Angew. Chem., Int. Ed. **43**, 3362 (2004).

[2] H. C. Joshi and L. Antonov, "Excited-state intramolecular proton transfer: A short introductory review," Molecules **26**, 1475 (2021).

[3] P. Zhou and K. Han, "Unraveling the detailed mechanism of excited-state proton transfer," Acc. Chem. Res. **51**, 1681–1690 (2018).

[4] A. P. Periyasamy, M. Vikova, and M. Vik, "A review of photochromism in textiles and its measurement," Text. Prog. **49**, 53–136 (2017).

[5] S.-J. Lim, J. Seo, and S. Y. Park, "Photochromic switching of excited-state intramolecular proton-transfer (ESIPT) fluorescence: A unique route to high-contrast memory switching and nondestructive readout," J. Am. Chem. Soc. **128**, 14542–14547 (2006).

[6] M. Irie, "Photochromism: Memories and switches introduction," Chem. Rev. **100**, 1683–1684 (2000).

[7] L. Chen, J.-W. Ye, H.-P. Wang, M. Pan, S.-Y. Yin, Z.-W. Wei, L.-Y. Zhang, K. Wu, Y.-N. Fan, and C.-Y. Su, "Ultrafast water sensing and thermal imaging by a metal-organic framework with switchable luminescence," Nat. Commun. **8**, 15985 (2017).

[8] H. Mishra, V. Misra, M. S. Mehata, T. C. Pant, and H. B. Tripathi, "Fluorescence studies of salicylic acid doped poly(vinyl alcohol) film as a water/Humidity sensor," J. Phys. Chem. A **108**, 2346–2352 (2004).

[9] M. Qin, Y. Huang, F. Li, and Y. Song, "Photochromic sensors: A versatile approach for recognition and discrimination," J. Mater. Chem. C **3**, 9265–9275 (2015).

[10] R. I. Cukier and D. G. Nocera, "Proton-coupled electron transfer," Annu. Rev. Phys. Chem. **49**, 337–369 (1998).

[11] S. Hammes-Schiffer and A. A. Stuchebrukhov, "Theory of coupled electron and proton transfer reactions," Chem. Rev. **110**, 6939–6960 (2010).

[12] D. Higelin and H. Sixl, "Spectroscopic studies of the photochromism of N-salicylideneaniline mixed crystals and glasses," Chem. Phys. **77**, 391–400 (1983).

[13] M. Ottolenghi and D. S. McClure, "Photochromism. I. The spectroscopy and energy levels of salicylideneaniline," J. Chem. Phys. **46**, 4613–4620 (1967).

[14] T. Rosenfeld, M. Ottolenghi, and A. Meyer, "Photochromic anils. Structure of photoisomers and thermal relaxation processes," Mol. Photochem. **5**, 39–60 (1973).

[15] K. Kownacki, A. Mordzinski, R. Wilbrandt, and A. Grabowska, "Laser-induced absorption and fluorescence studies of photochromic Schiff bases," Chem. Phys. Lett. **227**, 270–276 (1994).

[16] S. Pijeau, D. Foster, and E. G. Hohenstein, "Effect of nonplanarity on excited-state proton transfer and internal conversion in salicylideneaniline," J. Phys. Chem. A **122**, 5555–5562 (2018).

[17] J. M. Ortiz-Sánchez, R. Gelabert, M. Moreno, and J. M. Lluch, "Electronic-structure and quantum dynamical study of the photochromism of the aromatic Schiff base salicylideneaniline," J. Chem. Phys. **129**, 214308 (2008).

[18] M. Z. Zgierski and A. Grabowska, "Photochromism of salicylideneaniline (SA). How the photochromic transient is created: A theoretical approach," J. Chem. Phys. **112**, 6329–6337 (2000).

[19] L. Spörkel, G. Cui, and W. Thiel, "Photodynamics of Schiff base salicylideneaniline: Trajectory surface-hopping simulations," J. Phys. Chem. A **117**, 4574–4583 (2013).

[20] R. Destro, A. Gavezzotti, and M. Simonetta, "Salicylideneaniline," Acta Crystallogr., Sect. B: Struct. Crystallogr. Cryst. Chem. **34**, 2867–2869 (1978).

[21] T. Sekikawa, O. Schalk, G. Wu, A. E. Boguslavskiy, and A. Stolow, "Initial processes of proton transfer in salicylideneaniline studied by time-resolved photoelectron spectroscopy," J. Phys. Chem. A **117**, 2971–2979 (2013).

[22] T. Yuzawa, H. Takahashi, and H.-o. Hamaguchi, "Submicrosecond time-resolved infrared study on the structure of the photoinduced transient species of salicylideneaniline in acetonitrile," Chem. Phys. Lett. **202**, 221–226 (1993).

[23] M. Avadanei, N. Kuş, V. Cozan, and R. Fausto, "Structure and photochemistry of N-salicylidene-p-carboxyaniline isolated in solid argon," J. Phys. Chem. A **119**, 9121–9132 (2015).

[24] R. Nakagaki, T. Kobayashi, J. Nakamura, and S. Nagakura, "Spectroscopic and kinetic studies of the photochromism of *N*-salicylideneanilines and related compounds," Bull. Chem. Soc. Jpn. **50**, 1909–1912 (1977).

[25] M. Sliwa, N. Mouton, C. Ruckebusch, L. Poisson, A. Idrissi, S. Aloïse, L. Potier, J. Dubois, O. Poizat, and G. Buntinx, "Investigation of ultrafast photoinduced processes for salicylidene aniline in solution and gas phase: Toward a general photo-dynamical scheme," Photochem. Photobiol. Sci. **9**, 661–669 (2010).

[26] S. Mitra and N. Tamai, "Femtosecond spectroscopic study on photochromic salicylideneaniline," Chem. Phys. Lett. **282**, 391–397 (1998).

[27] S. Mitra and N. Tamai, "Dynamics of photochromism in salicylideneaniline: A femtosecond spectroscopic study," Phys. Chem. Chem. Phys. **5**, 4647–4652 (2003).

[28] P. F. Barbara, P. M. Rentzepis, and L. E. Brus, "Photochemical kinetics of salicylidenaniline," J. Am. Chem. Soc. **102**, 2786–2791 (1980).

[29] M. Ziółek, J. Kubicki, A. Maciejewski, R. Naskrecki, and A. Grabowska, "An ultrafast excited state intramolecular proton transfer (ESPIT) and photochromism of salicylideneaniline (SA) and its "double" analogue salicylaldehyde azine (SAA). A controversial case," Phys. Chem. Chem. Phys. **6**, 4682–4689 (2004).

[30] W. Rodríguez-Córdoba, J. S. Zugazagoitia, E. Collado-Fregoso, and J. Peon, "Excited state intramolecular proton transfer in Schiff bases. Decay of the locally excited enol state observed by femtosecond resolved fluorescence," J. Phys. Chem. A **111**, 6241–6247 (2007).

[31] M. C. Silfies, G. Kowzan, N. Lewis, and T. K. Allison, "Broadband cavity-enhanced ultrafast spectroscopy," Phys. Chem. Chem. Phys. **23**, 9743–9752 (2021).

[32] M. A. R. Reber, Y. Chen, and T. K. Allison, "Cavity-enhanced ultrafast spectroscopy: Ultrafast meets ultrasensitive," Optica **3**, 311–317 (2016).

[33] X. Li, M. A. R. Reber, C. Corder, Y. Chen, P. Zhao, and T. K. Allison, "High-power ultrafast Yb:fiber laser frequency combs using commercially available components and basic fiber tools," Rev. Sci. Instrum. **87**, 093114 (2016).

[34] M. C. Silfies, G. Kowzan, Y. Chen, N. Lewis, R. Hou, R. Baehre, T. Gross, and T. K. Allison, "Widely tunable cavity-enhanced frequency combs," Opt. Lett. **45**, 2123–2126 (2020).

[35] Y. Chen, M. C. Silfies, G. Kowzan, J. M. Bautista, and T. K. Allison, "Tunable visible frequency combs from a Yb-fiber-laser-pumped optical parametric oscillator," Appl. Phys. B **125**, 81 (2019).

[36] A. Mehmood, "First-principles simulations of ultrafast transient absorption spectrum," (unpublished).

[37] W.-T. Peng, B. S. Fales, and B. G. Levine, "Simulating electron dynamics of complex molecules with time-dependent complete active space configuration interaction," J. Chem. Theory Comput. **14**, 4129–4138 (2018).

[38] D. Miller, "Free jet sources," in *Atomic and Molecular Beam Methods*, edited by G. Scoles (Oxford University Press, 1988).

[39] I. H. M. van Stokkum, D. S. Larsen, and R. van Grondelle, "Global and target analysis of time-resolved spectra," Biochim. Biophys. Acta, Bioenerg. **1657**, 82–104 (2004).

[40]M. Ben-Nun, J. Quenneville, and T. J. Martínez, "*Ab initio* multiple spawning: Photochemistry from first principles quantum molecular dynamics," J. Phys. Chem. A **104**, 5161–5175 (2000).
[41]B. F. E. Curchod and T. J. Martínez, "*Ab initio* nonadiabatic quantum molecular dynamics," Chem. Rev. **118**, 3305–3336 (2018).
[42]B. G. Levine, A. S. Durden, M. P. Esch, F. Liang, and Y. Shu, "CAS without SCF—Why to use CASCI and where to get the orbitals," J. Chem. Phys. **154**, 090902 (2021).
[43]P. Slavíček and T. J. Martínez, "*Ab initio* floating occupation molecular orbital-complete active space configuration interaction: An efficient approximation to CASSCF," J. Chem. Phys. **132**, 234102 (2010).
[44]E. G. Hohenstein, "Analytic formulation of derivative coupling vectors for complete active space configuration interaction wavefunctions with floating occupation molecular orbitals," J. Chem. Phys. **145**, 174110 (2016).
[45]E. G. Hohenstein, M. E. F. Bouduban, C. Song, N. Luehr, I. S. Ufimtsev, and T. J. Martínez, "Analytic first derivatives of floating occupation molecular orbital-complete active space configuration interaction on graphical processing units," J. Chem. Phys. **143**, 014111 (2015).
[46]D. Hollas, L. Šištík, E. G. Hohenstein, T. J. Martínez, and P. Slavíček, "Nonadiabatic *ab initio* molecular dynamics with the floating occupation molecular orbital-complete active space configuration interaction method," J. Chem. Theory Comput. **14**, 339–350 (2018).
[47]S. Pijeau and E. G. Hohenstein, "Improved complete active space configuration interaction energies with a simple correction from density functional theory," J. Chem. Theory Comput. **13**, 1130–1146 (2017).
[48]M. A. Rohrdanz, K. M. Martins, and J. M. Herbert, "A long-range-corrected density functional that performs well for both ground-state properties and time-dependent density functional theory excitation energies, including charge-transfer excited states," J. Chem. Phys. **130**, 054112 (2009).
[49]H. R. Hudock, B. G. Levine, A. L. Thompson, H. Satzger, D. Townsend, N. Gador, S. Ullrich, A. Stolow, and T. J. Martínez, "*Ab initio* molecular dynamics and time-resolved photoelectron spectroscopy of electronically excited uracil and thymine," J. Phys. Chem. A **111**, 8500–8508 (2007).
[50]R. Borrego-Varillas, A. Nenov, P. Kabaciński, I. Conti, L. Ganzer, A. Oriana, V. K. Jaiswal, I. Delfino, O. Weingart, C. Manzoni, I. Rivalta, M. Garavelli, and G. Cerullo, "Tracking excited state decay mechanisms of pyrimidine nucleosides in real time," Nat. Commun. **12**, 7285 (2021).
[51]P. Chakraborty, Y. Liu, S. McClung, T. Weinacht, and S. Matsika, "Time resolved photoelectron spectroscopy as a test of electronic structure and nonadiabatic dynamics," J. Phys. Chem. Lett. **12**, 5099–5104 (2021).
[52]M. A. Kochman, B. Durbeej, and A. Kubas, "Simulation and analysis of the transient absorption spectrum of 4-(N,N-dimethylamino)benzonitrile (DMABN) in acetonitrile," J. Phys. Chem. A **125**, 8635–8648 (2021).
[53]D. Avagliano, M. Bonfanti, A. Nenov, and M. Garavelli, "Automatized protocol and interface to simulate QM/MM time-resolved transient absorption at TD-DFT level with COBRAMM," J. Comput. Chem. **43**, 1641–1655 (2022).
[54]A. S. Durden and B. G. Levine, "Floquet time-dependent configuration interaction for modeling ultrafast electron dynamics," J. Chem. Theory Comput. **18**, 795–806 (2022).
[55]X. Li, N. Govind, C. Isborn, A. E. DePrince, and K. Lopata, "Real-time time-dependent electronic structure theory," Chem. Rev. **120**, 9951–9993 (2020).
[56]U. De Giovannini, G. Brunetto, A. Castro, J. Walkenhorst, and A. Rubio, "Simulating pump–probe photoelectron and absorption spectroscopy on the attosecond timescale with time-dependent density functional theory," ChemPhysChem **14**, 1363–1376 (2013).
[57]A. Bruner, D. LaMaster, and K. Lopata, "Accelerated broadband spectra using transition dipole decomposition and padé approximants," J. Chem. Theory Comput. **12**, 3741–3750 (2016).
[58]D. R. Nascimento and A. E. I. DePrince, "Linear absorption spectra from explicitly time-dependent equation-of-motion coupled-cluster theory," J. Chem. Theory Comput. **12**, 5834–5840 (2016).
[59]J. J. Goings, P. J. Lestrange, and X. Li, "Real-time time-dependent electronic structure theory," Wiley Interdiscip. Rev.: Comput. Mol. Sci. **8**, e1341 (2018).
[60]I. S. Ufimtsev and T. J. Martinez, "Quantum chemistry on graphical processing units. 3. Analytical energy gradients, geometry optimization, and first principles molecular dynamics," J. Chem. Theory Comput. **5**, 2619–2628 (2009).
[61]S. Seritan, C. Bannwarth, B. S. Fales, E. G. Hohenstein, C. M. Isborn, S. I. L. Kokkila-Schumacher, X. Li, F. Liu, N. Luehr, J. W. Snyder, Jr., C. Song, A. V. Titov, I. S. Ufimtsev, L.-P. Wang, and T. J. Martínez, "TeraChem: A graphical processing unit-accelerated electronic structure package for large-scale *ab initio* molecular dynamics," Wiley Interdiscip. Rev.: Comput. Mol. Sci. **11**, e1494 (2021).
[62]B. S. Fales and B. G. Levine, "Nanoscale multireference quantum chemistry: Full configuration interaction on graphical processing units," J. Chem. Theory Comput. **11**, 4708–4716 (2015).
[63]P. M. Felker and A. H. Zewail, "Purely rotational coherence effect and time-resolved sub-Doppler spectroscopy of large molecules. I. Theoretical," J. Chem. Phys. **86**, 2460–2482 (1987).
[64]J. Zhao, S. Ji, Y. Chen, H. Guo, and P. Yang, "Excited state intramolecular proton transfer (ESIPT): From principal photophysics to the development of new chromophores and applications in fluorescent molecular probes and luminescent materials," Phys. Chem. Chem. Phys. **14**, 8803–8817 (2012).
[65]S. Lochbrunner, A. Szeghalmi, K. Stock, and M. Schmitt, "Ultrafast proton transfer of 1-hydroxy-2-acetonaphthone: Reaction path from resonance Raman and transient absorption studies," J. Chem. Phys. **122**, 244315 (2005).
[66]P. Wnuk, G. Burdziński, M. Sliwa, M. Kijak, A. Grabowska, J. Sepioł, and J. Kubicki, "From ultrafast events to equilibrium–uncovering the unusual dynamics of ESIPT reaction: The case of dually fluorescent diethyl-2,5-(dibenzoxazolyl)-hydroquinone," Phys. Chem. Chem. Phys. **16**, 2542–2552 (2014).
[67]S. Lee, J. Lee, and Y. Pang, "Excited state intramolecular proton transfer of 1,2-dihydroxyanthraquinone by femtosecond transient absorption spectroscopy," Curr. Appl. Phys. **15**, 1492–1499 (2015).
[68]U. Buck and R. Krohne, "Cluster size determination from diffractive He atom scattering," J. Chem. Phys. **105**, 5408–5415 (1996).
[69]M. Barbatti, G. Granucci, M. Persico, and H. Lischka, "Semiempirical molecular dynamics investigation of the excited state lifetime of ethylene," Chem. Phys. Lett. **401**, 276–281 (2005).
[70]H. Tao, T. K. Allison, T. W. Wright, A. M. Stooke, C. Khurmi, J. van Tilborg, Y. Liu, R. W. Falcone, A. Belkacem, and T. J. Martinez, "Ultrafast internal conversion in ethylene. I. The excited state lifetime," J. Chem. Phys. **134**, 244306 (2011).
[71]E. Engel, K. Schmidt, D. Beljonne, J.-L. Brédas, J. Assa, H. Fröb, K. Leo, and M. Hoffmann, "Transient absorption spectroscopy and quantum-chemical studies of matrix-isolated perylene derivatives," Phys. Rev. B **73**, 245216 (2006).
[72]M. Gühr, M. Bargheer, P. Dietrich, and N. Schwentner, "Predissociation and vibrational relaxation in the B state of I_2 in a Kr matrix," J. Phys. Chem. A **106**, 12002–12011 (2002).
[73]R. Thon, W. Chin, J.-P. Galaup, A. Ouvrard, B. Bourguignon, and C. Crépin, "Vibrational perturbations of $W(CO)_6$ trapped in a molecular lattice probed by linear and nonlinear spectroscopy," J. Phys. Chem. A **117**, 8145–8156 (2013).